THE MEAN NUMBER OF EXTRA MICROIMAGE PAIRS FOR MACROLENSED QUASARS

JONATHAN GRANOT,[1] PAUL L. SCHECHTER,[1,2] AND JOACHIM WAMBSGANSS[3]

ABSTRACT

When a gravitationally lensed source crosses a caustic, a pair of images is created or destroyed. We calculate the mean number of such pairs of microimages $\langle n \rangle$ for a given macroimage of a gravitationally lensed point source due to microlensing by the stars of the lensing galaxy. This quantity was calculated by Wambsganss, Witt, and Schneider in 1992 for the case of zero external shear, $\gamma = 0$, at the location of the macroimage. Since in realistic lens models a nonzero shear is expected to be induced by the lensing galaxy, we extend this calculation to a general value of γ. We find a complex behavior of $\langle n \rangle$ as a function of γ and the normalized surface mass density in stars, κ_*. Specifically, we find that at high magnifications, where the average total magnification of the macroimage is $\langle \mu \rangle = |(1 - \kappa_*)^2 - \gamma^2|^{-1} \gg 1$, $\langle n \rangle$ becomes correspondingly large and is proportional to $\langle \mu \rangle$. The ratio $\langle n \rangle / \langle \mu \rangle$ is largest near the line $\gamma = 1 - \kappa_*$, where the magnification $\langle \mu \rangle$ becomes infinite, and its maximal value is 0.306. We compare our semianalytic results for $\langle n \rangle$ with the results of numerical simulations and find good agreement. We find that the probability distribution for the number of extra microimage pairs is reasonably described by a Poisson distribution with a mean value of $\langle n \rangle$ and that the width of the macroimage magnification distribution tends to be largest for $\langle n \rangle \sim 1$.

Subject headings: dark matter — gravitational lensing — quasars: general

1. INTRODUCTION

Gravitational microlensing by the stars of a lensing galaxy can have a large effect on the magnification of lensed sources (Chang & Refsdal 1979; Young 1981; Paczyński 1986). Since the macroimages of multiply imaged sources are typically located in relatively dense star fields of the lensing galaxy, microlensing is quite common in such systems. The typical angular separation between the microimages of a cosmological source due to a stellar mass microlens is of the order of 1 μas, which is far too small to be resolved. For the time being, the only observable manifestation of microlensing is to change the magnification of the macroimage relative to the average magnification that is predicted for the smoothed-out surface mass density profile of the galaxy.

The first observational evidence for quasar microlensing was found by Irwin et al. (1989) in the quadruple system Q2237+0305, which has subsequently been monitored by many groups (Corrigan et al. 1991; Burud et al. 1998; Lewis et al. 1998, Woźniak et al. 2000a, 2000b). In particular, the latest results show that all four quasar images vary dramatically, going up and down by more than 1 mag on timescales of less than a year. The fact that individual (caustic crossing) events can be clearly distinguished allows us to put upper limits on the source size (Wambsganss, Paczyński, & Schneider 1990; Yonehara 1999, 2001; Wyithe et al. 2000).

In the double quasar Q0957+561, originally there was an almost linear change detected in the (time shifted) brightness ratio between the two images ($\Delta(m_A - m_B) \approx 0.25$ mag over 5 yr), which was interpreted as microlensing by solar-type stars. However, since about 1991, this ratio has stayed more or less "constant" within about 0.05 mag, so not much microlensing has been going on in this system recently (Schild 1996; Pelt et al. 1998). Nevertheless, even the "lack of microlensing" in this system can be used to put limits on compact dark matter in the halo of the lensing galaxy (Wambsganss et al. 2000).

A number of other multiple-quasar systems are being monitored more or less regularly, with some showing indications of microlensing, e.g., H1413+117 (Østensen et al. 1997), B0218+357 (Jackson, Xanthopoulos, & Browne 2000), or HE 1104−1805 (Gil-Merino, Wisotzki, & Wambsganss 2002; Schechter et al. 2003). For a recent review on quasar microlensing, see Wambsganss (2001).

Microlensing has recently been suggested as the source of short-timescale low-level variability in the time-delayed light curves of multiple images of quasars (Wyithe & Loeb 2002) and might help in studying the properties of broadline clouds in quasars. A better understanding of the microlensing by stars in galaxies would provide a better handle on the probability distribution for the microlensing of cosmological sources (Wyithe & Turner 2002) that is relevant for gamma-ray bursts (GRBs), especially in light of a possible microlensing event that was observed in the optical and near-IR light curve of the afterglow of GRB 000301C (Garnavich, Loeb, & Stanek 2000; Gaudi, Granot, & Loeb 2001; Koopmans & Wambsganss 2001).

Another example in which microlensing may play an important role is in explaining the flux ratio anomalies observed in close pairs of images of quadruply lensed quasars (Schechter & Wambsganss 2002). Such systems are usually modeled using a simple smooth surface mass density profile for the galaxy, possibly with the addition of an external shear. While these models successfully reproduce the observed locations of the macroimages, the flux ratios they predict are quite often in poor agreement with observations. Specifically, the theoretical flux ratio for a close pair of highly magnified macroimages is 1 : 1, while observations

[1] Institute for Advanced Study, Olden Lane, Princeton, NJ 08540.

[2] Department of Physics, 77 Massachusetts Avenue, Massachusetts Institute of Technology, Cambridge, MA 02139.

[3] Universität Potsdam, Institut für Physik, Am Neuen Palais 10, 14467 Potsdam, Germany.

show a difference of up to 1 mag. For example, MG 0414+0534 has an observed flux ratio of 2 : 1 in the optical (Hewitt et al. 1992; Schechter & Moore 1993), while in the radio, the flux ratio is 1 : 1 (Trotter, Winn, & Hewitt 2000). There are also alternative explanations for these flux ratio anomalies, such as intervening dust (Lawrence et al. 1995) or millilensing by galactic substructure (Mao & Schneider 1998; Metcalf & Madau 2001; Dalal & Kochanek 2002; Chiba 2002). The study of microlensing can help distinguish between these alternative explanations and may be useful in constraining the substructure of galaxies.

In many cases the study of microlensing cannot be done analytically, and much of the work is done using numerical simulations. The magnification distributions of the macro-image (MDMs) are particularly important for understanding the observed properties of lensed systems. The latter have been calculated for a wide range of parameters using numerical simulations (Wambsganss 1992; Rauch et al. 1992; Lewis & Irwin 1995, 1996; Schechter & Wambsganss 2002). While simulations are applicable to a wide range of problems and are in many cases the only available technique, they are usually time consuming and do not always provide a qualitative understanding of the results. Specifically, they do not seem to provide an explanation for the detailed structure that is present in the MDMs that they produce.

In a recent paper, Schechter & Wambsganss (2002) explained the flux ratio anomalies as resulting from a different qualitative behavior of the MDMs for macrominima and macro–saddle points in the arrival-time surface that results in a larger probability for demagnification (relative to the average magnification) of saddle points compared to minima. This is in agreement with the observations of MG 0414+0534 and four other recently discovered quadruple systems (Reimers et al. 2002; Inada et al. 2002; S. Burles et al. 2003, in preparation; P. L. Schechter et al. 2003, in preparation), in all of which the fainter image in a pair corresponds to a saddle point, while the brighter image corresponds to a minimum.

The structure of the MDMs seems to be tightly related to the probability distribution for the number of extra micro-image pairs (EIPs) corresponding to a given macroimage (Rauch et al. 1992). This can be expected, since the magnification of the macroimage is simply the sum of the magnifications of all the microimages that it is composed of. An analytic expression for the mean number of EIPs was derived by Wambsganss, Witt, & Schneider (1992, hereafter WWS92) for the case of zero external shear. In § 2 we generalize this result for arbitrary values of the external shear and obtain a semianalytic expression. More detailed expressions are provided in the Appendix, along with an analytic result for the case of equal shear and convergence in stars. In § 3 we compare our analytic results with numerical simulations and find good agreement. We also show that the probability distribution for the number of EIPs is reasonably described by a Poisson distribution. The possible implications of our results are discussed in § 4.

2. ANALYTIC RESULTS

In this section we calculate the mean number of positive parity microimages $\langle N \rangle$ and the mean number of extra microimage pairs (EIPs) $\langle n \rangle$ that are induced by the random star field of the lensing galaxy near the location of a macro-

image. The macroimages are located at stationary points (i.e., minima, saddle points, or maxima) of the time-delay (Fermat) surface of the smoothed-out surface mass density distribution of the lensing galaxy. The source size is assumed to be small compared to the Einstein radius of the stars in the galaxy and compared to the typical distance between caustics, so that we can assume a point source. In this limit the probability distribution of the random shear caused by the star field and the resulting distributions of the number of microimages and total magnification of the macro-image are independent of the mass spectrum of the stars (Schneider & Weiss 1988). The remaining parameters on which the microlensing characteristics in this case might still depend are the normalized surface mass density in the stars, κ_*, and in a smooth component (dark matter), κ_c, as well as the large-scale shear of the galaxy γ. However, Paczyński (1986) has shown that such a model is always equivalent to a model with effective convergence and shear given by

$$\kappa_*^{\rm eff} = \frac{\kappa_*}{1 - \kappa_c}, \quad \gamma^{\rm eff} = \frac{\gamma}{1 - \kappa_c} \tag{1}$$

and with no smooth component ($\kappa_c^{\rm eff} \equiv 0$). The effective magnification in this model is related to the true magnification by $\mu^{\rm eff} = \mu(1 - \kappa_c)^2$. Therefore, without loss of generality, we restrict ourselves to $\kappa_c = 0$ while letting κ_* and γ vary.

Each pair of microimages (EIPs) consists of a saddle point and a minimum and thereby includes one positive-parity image. For a macrominimum there is also an additional positive-parity microimage corresponding to the global minimum. Therefore, $n = N - 1$ for a macro-minimum and $n = N$ otherwise, where n is the number of EIPs and N is the number of positive-parity microimages. This also carries through to the average values of these quantities:

$$\langle n \rangle = \begin{cases} \langle N \rangle - 1, & \kappa_* + \gamma < 1 , \\ \langle N \rangle, & \kappa_* + \gamma > 1 . \end{cases} \tag{2}$$

It is therefore sufficient to calculate one of these quantities in order to determine the other. The values of $\langle N \rangle$ and $\langle n \rangle$ for the case of zero external shear ($\gamma = 0$) were calculated by WWS92. In this work we follow their analysis and generalize their result to the case of a nonzero shear γ. The average total magnification of the macroimage is given by

$$\langle \mu \rangle = \frac{1}{|(1 - \kappa_*)^2 - \gamma^2|} . \tag{3}$$

Since the magnification is solely due to area distortion, flux conservation implies that a sufficiently large area $\mathscr{A}_d$ in the deflector plane will be (backward) mapped onto an area $\mathscr{A}_s = \mathscr{A}_d / \langle \mu \rangle$ in the source plane (when projected onto the deflector plane, so that it extends to the same solid angle as seen from the observer). The mean number of positive-parity microimages $\langle N \rangle$ is equal to the multiplicity q by which regions of positive parity within $\mathscr{A}_d$, when mapped onto $\mathscr{A}_s$, cover $\mathscr{A}_s$.

The probability distribution of the random shear produced by the stars is given by

$$p(\kappa_*, \ S_1, \ S_2) = \frac{\kappa_*}{2\pi \left(\kappa_*^2 + S_1^2 + S_2^2 \right)^{3/2}} \tag{4}$$

(Nityananda & Ostriker 1984; Schneider, Ehlers, & Falco 1992, p. 329), where S_1 and S_2 are the two components of the *internal* shear. Since we assume that $\kappa_c = 0$ and that the stars are point masses, the convergence vanishes everywhere (except at the locations of the stars, where it is infinite, but these form a set of measure zero for any finite area on the deflector plane), and the local magnification at a given location in the star field is just due to the shear at that point:

$$\mu(\gamma,\ S_1,\ S_2) = \frac{1}{1 - (\gamma + S_1)^2 - S_2^2}\ , \qquad (5)$$

where for convenience we have chosen S_1 to lie in the direction of the external shear γ. The area $da_d = \mathscr{A}_d p(\kappa_*,\ S_1,\ S_2)\, dS_1\, dS_2$ within $\mathscr{A}_d$, where the shear lies between $(\gamma + S_1,\ S_2)$ and $(\gamma + S_1 + dS_1,\ S_2 + dS_2)$, is mapped onto the area $da_s = da_d / \mu(\gamma,\ S_1,\ S_2)$.

Therefore,

$$\langle N \rangle = q = \frac{1}{\mathscr{A}_s} \int_{\mu > 0} \frac{da_d}{\mu}$$

$$= \langle \mu \rangle \int \int_{\mu > 0} \frac{p(\kappa_*,\ S_1,\ S_2)\, dS_1\, dS_2}{\mu(\gamma,\ S_1,\ S_2)}$$

$$= \frac{\kappa_*}{2\pi |(1 - \kappa_*)^2 - \gamma^2|} \int_{-1-\gamma}^{1-\gamma} dS_1$$

$$\times \int_{-\sqrt{1-(\gamma+S_1)^2}}^{\sqrt{1-(\gamma+S_1)^2}} dS_2 \ \frac{1 - (\gamma + S_1)^2 - S_2^2}{\left(\kappa_*^2 + S_1^2 + S_2^2\right)^{3/2}}\ . \qquad (6)$$

This integral can be evaluated analytically. However, the resulting expression is long and cumbersome, so we prefer not to write it down explicitly. Instead, we show contour plots of $\langle n \rangle$ and $\langle n \rangle / \langle \mu \rangle$ in Figure 1 and provide the values
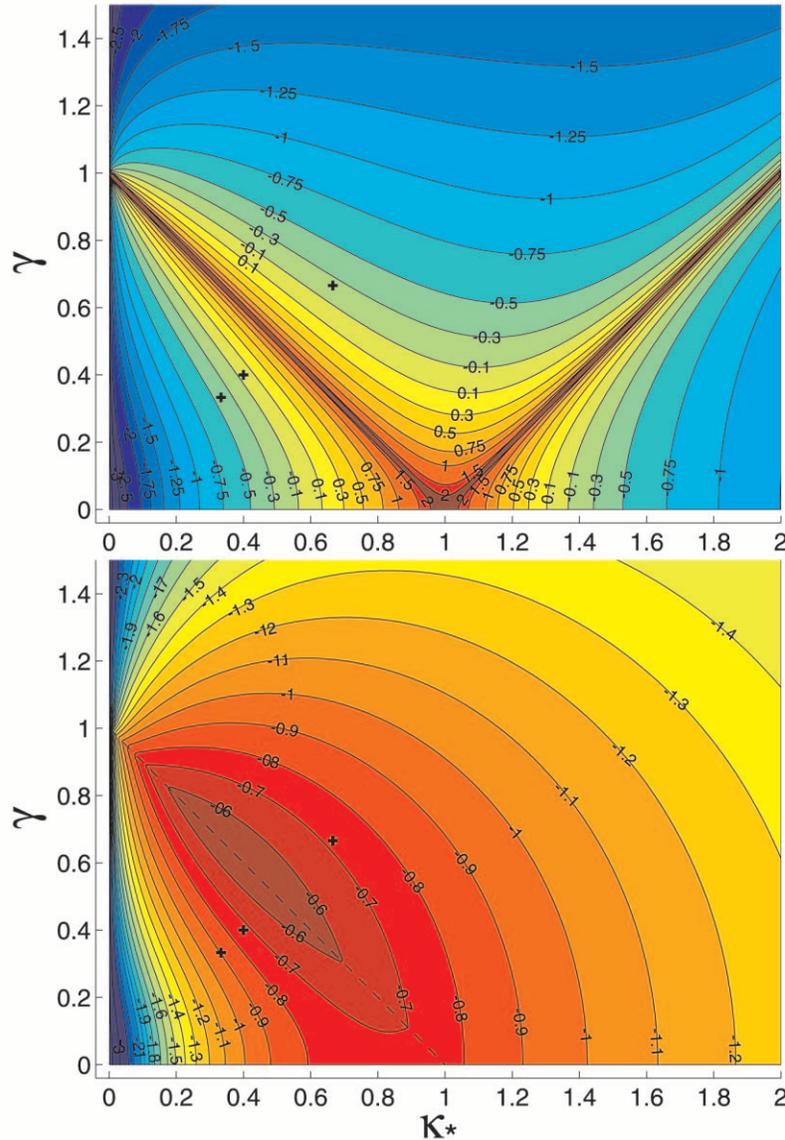

Fig. 1.—Contour plots of $\log_{10}(\langle n \rangle)$ (*top*) and $\log_{10}(\langle n \rangle / \langle \mu \rangle)$ (*bottom*) in the κ_*-γ plane. The dashed line in the bottom panel shows the line of infinite magnification $\gamma = 1 - \kappa_*$ along which there is a "ridge" in $\langle n \rangle / \langle \mu \rangle$, while the three plus symbols in both panels mark the values used in our three simulations: $\kappa_* = \gamma = 0.333, 0.400,$ and 0.666.

TABLE 1

THE RATIO $\langle N \rangle / \langle \mu \rangle$

	$\langle N \rangle / \langle \mu \rangle$												
γ	$\kappa_* = 0$	0.1	0.2	0.3	0.4	0.5	0.6	0.7	0.8	0.9	1	1.2	1.5
0......	1	0.8190	0.6721	0.5536	0.4584	0.3820	0.3206	0.2711	0.2310	0.1983	0.1716	0.1311	0.0917
0.1...	0.99	0.8105	0.6650	0.5478	0.4537	0.3782	0.3176	0.2687	0.2292	0.1969	0.1704	0.1303	0.0913
0.2...	0.96	0.7850	0.6438	0.5305	0.4398	0.3672	0.3089	0.2618	0.2237	0.1926	0.1670	0.1281	0.0901
0.3...	0.91	0.7428	0.6089	0.5022	0.4171	0.3492	0.2947	0.2507	0.2149	0.1856	0.1615	0.1246	0.0882
0.4...	0.84	0.6841	0.5608	0.4635	0.3864	0.3250	0.2756	0.2357	0.2031	0.1763	0.1540	0.1198	0.0856
0.5...	0.75	0.6095	0.5005	0.4156	0.3487	0.2955	0.2526	0.2176	0.1889	0.1650	0.1450	0.1140	0.0824
0.6...	0.64	0.5200	0.4296	0.3602	0.3058	0.2621	0.2266	0.1973	0.1728	0.1522	0.1348	0.1073	0.0787
0.7...	0.51	0.4173	0.3505	0.2999	0.2596	0.2266	0.1989	0.1756	0.1557	0.1386	0.1239	0.1001	0.0746
0.8...	0.36	0.3048	0.2678	0.2383	0.2131	0.1908	0.1711	0.1536	0.1382	0.1245	0.1125	0.0925	0.0702
0.9...	0.19	0.1907	0.1886	0.1805	0.1692	0.1568	0.1444	0.1323	0.1211	0.1107	0.1012	0.0848	0.0657
1......	0	0.0974	0.1236	0.1314	0.1310	0.1265	0.1200	0.1126	0.1049	0.0974	0.0902	0.0771	0.0611
1.2...	0	0.0303	0.0534	0.0682	0.0764	0.0801	0.0808	0.0795	0.0770	0.0739	0.0703	0.0628	0.0521
1.5...	0	0.0111	0.0212	0.0298	0.0366	0.0415	0.0448	0.0468	0.0477	0.0478	0.0472	0.0449	0.0400

NOTES.—The ratio of the mean number of positive-parity microimages $\langle N \rangle$ and the mean total magnification $\langle \mu \rangle$ for different values of the normalized surface mass density in stars κ_* and the external shear γ, calculated using eqs. (6), (A1), (A3), and (A5).

of $\langle N \rangle / \langle \mu \rangle$ at representative points of (κ_*, γ) in Table 1. In the Appendix we reduce the expression in equation (6) to a one-dimensional integral in two different ways (so that $\langle N \rangle$ can be easily evaluated numerically) and provide an analytic expression for the case in which $\gamma = \kappa_*$. For $\gamma = 0$, equation (6) reduces to a simple analytic expression (WWS92):

$$\frac{\langle N \rangle}{\langle \mu \rangle} = \langle N \rangle (1 - \kappa_*)^2 = 1 + 2\kappa_*^2 - 2\kappa_* \sqrt{1 + \kappa_*^2} . \quad (7)$$

For $\kappa_* = 0$, there are no extra images due to stars, and we have either one positive-parity image for a macrominimum ($N = \langle N \rangle = 1$ for $\gamma < 1$) or none for a macro–saddle point ($N = \langle N \rangle = 0$ for $\gamma > 1$). Hence, for $\kappa_* = 0$, we have

$$\frac{\langle N \rangle}{\langle \mu \rangle} = \langle N \rangle (1 - \gamma^2) = \begin{cases} 1 - \gamma^2 , & \gamma < 1 , \\ 0 , & \gamma \geq 1 . \end{cases} \quad (8)$$

As can be seen from equation (6), the ratio $\langle N \rangle / \langle \mu \rangle$ remains finite and varies smoothly with γ and κ_* near the lines of infinite average total magnification $\langle \mu \rangle$ in the γ-κ_* plane (i.e., $\gamma = |1 - \kappa_*|$). Together with equation (2), this implies the same for the ratio $\langle n \rangle / \langle \mu \rangle$ along the line $\gamma = \kappa_* - 1$, while along the line $\gamma = 1 - \kappa_*$ it is continuous, but its derivative is discontinuous in any direction that is not along this line (as can be seen in Fig. 1 [bottom]).

Furthermore, $\langle n \rangle / \langle \mu \rangle$ decreases on either side of the line $\gamma = 1 - \kappa_*$ and therefore attains its maximal value along this line: $(\langle n \rangle / \langle \mu \rangle)_{\max} = 0.306136$ at $(\kappa_*, \gamma) = (0.37895, 0.62105)$. For $\langle \mu \rangle \gg 1$ ($\gamma \approx |1 - \kappa_*|$), small changes in γ or κ_* can cause large changes in $\langle \mu \rangle$ and $\langle n \rangle$, while the ratios $\langle n \rangle / \langle \mu \rangle$ or $\langle N \rangle / \langle \mu \rangle$ remain approximately constant. In this region, when crossing the line of infinite magnification $\gamma = 1 - \kappa_*$ from a macrominimum ($\gamma < 1 - \kappa_*$) to a macro–saddle point ($\gamma > 1 - \kappa_*$), $\langle N \rangle$ decreases by 1 (corresponding to the macrominimum that disappears), but since $\langle N \rangle$ is infinite at this line, this amounts to a zero fractional change in $\langle N \rangle$.

3. COMPARISON WITH NUMERICAL SIMULATIONS

In this section we compare the analytic results of § 2 with the results of numerical simulations. Combining a ray-shooting code (Wambsganss 1990, 1999) with a program that detects the location of the caustics (Witt 1993) as in WWS92, we extract additional information on image multiplicity and magnification. Whenever the source crosses a caustic, a pair of images consisting of a micro–saddle point and a microminimum are created or destroyed. Each simulation is based on a particular realization of the random star field that determines a caustic network in the source plane and in principle determines the number of such EIPs at any point in the source plane. In order to calculate the average number of EIPs $\langle n \rangle$ from the results of a simulation, we identify the regions with different numbers of EIPs n on the source plane and calculate the fraction f_n of the source plane that they cover, which is equal to the probability p_n of having n EIPs at a random location on the source plane. This is illustrated in Figure 2. Pixels in the source plane that are crossed by caustics (which are colored in yellow in Fig. 2) are attributed to the corresponding higher image number. There are also parts of the source plane for which it is very difficult to uniquely identify n (corresponding to the black regions in Fig. 2) because of the occasionally complex caustic structure, combined with the finite pixel size of the simulation. These regions are left out when calculating f_n. The "unidentified" regions correspond to $\sim 1\%$ of the source plane, and a large fraction of these regions probably correspond to relatively high values of n. However, as we do not know exactly what distribution of multiplicity n we should assign to these regions, and lacking a better option, we simply assign to them the same distribution as the identified regions:

$$p_n = \frac{f_n}{\sum_{n'} f_{n'}} . \quad (9)$$

This is equivalent to leaving out the unidentified regions entirely and normalizing the probability distribution of p_n. The average number of EIPs for the simulation is then given by

$$\langle n \rangle_{\text{sim}} = \sum_n n p_n . \quad (10)$$

Since we have simple analytic expressions for $\langle n \rangle$ for $\gamma = 0$ (WWS92; eq. [7]) and for $\kappa_* = 0$ (eq. [8]), we chose
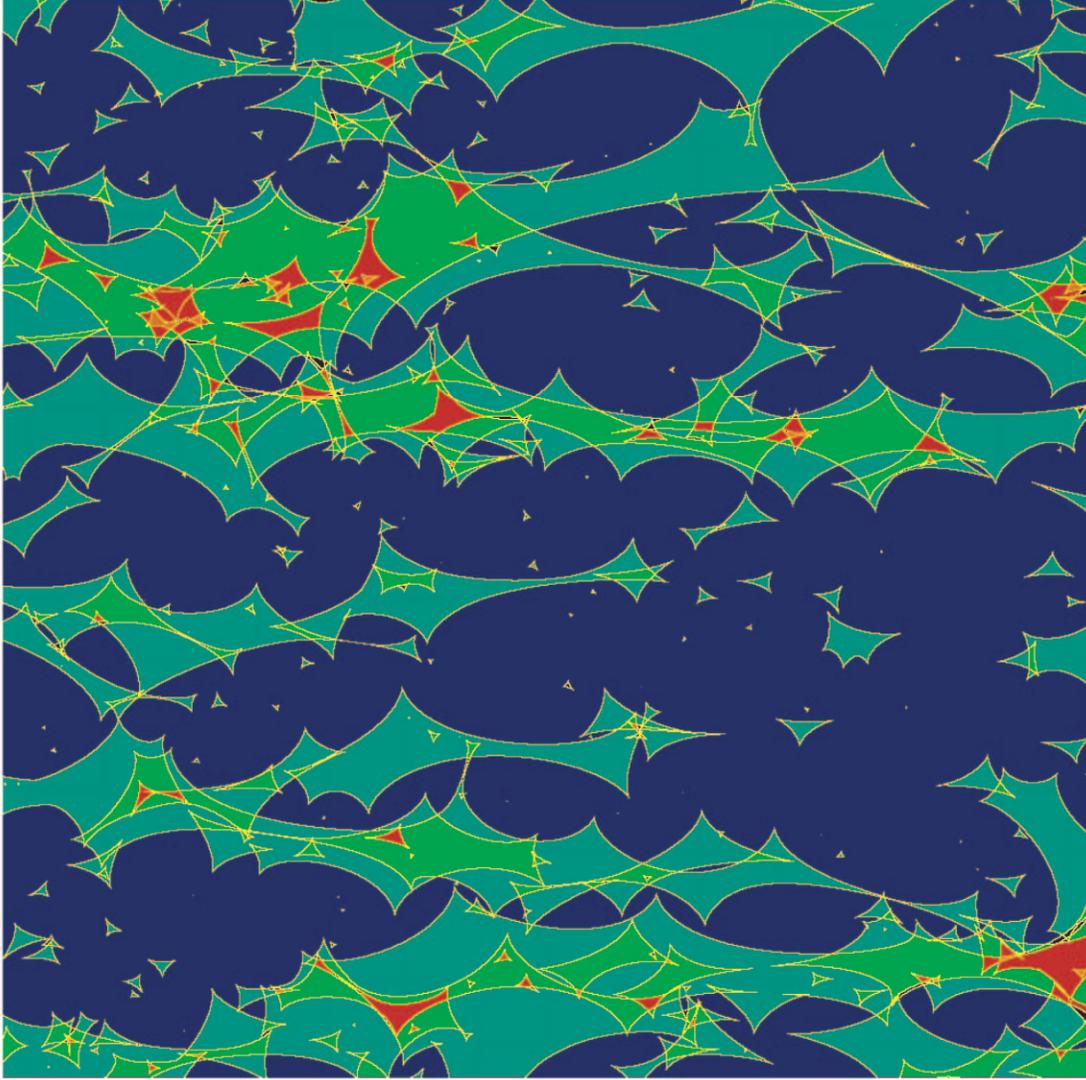
Fig. 2.—Map of the number of EIPs n in the source plane, for the simulation with $\gamma = \kappa_* = 0.666$. The regions in dark blue, turquoise, green, red, and orange correspond to $n = 0, 1, 2, 3$, and 4, respectively. The yellow lines represent the caustics, while regions for which n could not be determined are in black.

values of (κ_*, γ) along the line $\kappa_* = \gamma$ for the simulations, so they would serve as a good check for our analytic results. An additional advantage of this choice is that it corresponds to the interesting case of a singular isothermal sphere (for $\kappa_c = 0$). We performed three simulations, two for macrominima ($\kappa_* = \gamma = 0.333, 0.400$ with $\langle \mu \rangle \simeq 3, 5$) and one for a macro–saddle point ($\kappa_* = \gamma = 0.666$ with $\langle \mu \rangle \simeq 3$). The results of the simulations are shown in Tables 2 and 3. For $\kappa_* = \gamma = 0.333, 0.400$, and 0.666, $\langle n \rangle_{\text{sim}}$ is 3.7%, 3.3%, and 7.7%, respectively, lower than the analytic result $\langle n \rangle$ from § 2 (denoted by $\langle n \rangle_{\text{th}}$ in Table 2). The values of $\langle n \rangle_{\text{sim}}$ in Table 2 were calculated according to equation (10), which assigns the p_n distribution of the regions with identified image multiplicity n in the source plane to the unidentified regions. However, as mentioned above, the unidentified regions are typically related to complicated caustic structures and are hence more likely to contribute to larger values of n compared to the identified regions. If the average n of the unidentified regions is, for instance, 5, this would make $\langle n \rangle_{\text{sim}}$ 1.1% higher, 2.6% higher, and 1.1% lower than $\langle n \rangle$ for $\kappa_* = \gamma = 0.333, 0.400$, and 0.666, respectively. The latter

should assume values of 3.96, 3.19, and 5.70 for $\kappa_* = \gamma = 0.333, 0.400$, and 0.666, respectively, in order for $\langle n \rangle_{\text{sim}}$ to be exactly equal to $\langle n \rangle$. One should also keep in mind the "cosmic" variance, i.e., the fluctuations between the results of different simulations for the same κ_* and γ due to different statistical realizations of the star field over a

TABLE 2
NUMERICAL SIMULATIONS VERSUS THEORY

$\kappa_* = \gamma$	$\langle n \rangle_{\text{sim}}$	$\langle n \rangle_{\text{th}}$	$\langle \mu \rangle_{\text{sim}}$	$\langle \mu \rangle_{\text{th}}$
0.333	0.367	0.3806	2.902	2.994
0.400	0.901	0.9320	4.992	5.000
0.666	0.531	0.5759	2.907	3.012

NOTES.—The first column labels the simulation through the values of the normalized surface mass density in stars κ_* and the external shear γ. The next two columns provide the average number of EIPs calculated from the simulation (according to eq. [10]) $\langle n \rangle_{\text{sim}}$ and the theoretical prediction for this quantity $\langle n \rangle_{\text{th}}$, calculated using eqs. (2) and (6). The last two columns are the average magnification of the simulation $\langle \mu \rangle_{\text{sim}}$ and the theoretical average magnification $\langle \mu \rangle_{\text{th}}$ (from eq. [3]).

TABLE 3
RESULTS OF NUMERICAL SIMULATIONS

$\kappa_* = \gamma$	n	f_n	$\sum_{i=0}^{n} f_i$	p_n	$\langle \mu \rangle_n$
0.333	0	0.690800	0.690800	0.693511	1.780
	1	0.251230	0.942030	0.252216	4.903
	2	0.049298	0.991328	0.049492	6.999
	3	0.003878	0.995206	0.003893	11.62
	4	0.000777	0.995983	0.000780	15.07
	5	0.000108	0.996091	0.000108	17.14
0.400	0	0.362692	0.362692	0.367695	2.387
	1	0.412717	0.775409	0.418409	5.352
	2	0.164497	0.939906	0.166766	7.726
	3	0.039863	0.979769	0.040413	10.51
	4	0.005832	0.985601	0.005912	13.16
	5	0.000749	0.986350	0.000759	16.65
	6	0.000045	0.986395	0.000046	26.33
0.666	0	0.584765	0.584765	0.589852	1.239
	1	0.300253	0.885018	0.302865	4.497
	2	0.093123	0.978141	0.093933	6.807
	3	0.012753	0.990894	0.012864	9.935
	4	0.000482	0.991376	0.000486	14.90

NOTES.—The first column labels the simulation through the values of $\kappa_* = \gamma$. The remaining five columns are the number of EIPs n, the corresponding fraction of the source plane f_n, its cumulative value up to n, its normalized value p_n calculated according to eq. (9), and the mean magnification of regions with n EIPs, $\langle \mu \rangle_n$ (which are marked by inverted triangles in Fig. 4).

finite region in the deflector plane. We therefore conclude that there is good agreement between the results of the numerical simulations and our analytic results for the average number of EIPs $\langle n \rangle$.

The average total magnifications from the simulations, $\langle \mu \rangle_{\rm sim}$, are 3.1%, 0.16%, and 3.5% lower than their theoretical values for $\kappa_* = \gamma = 0.333$, 0.400, and 0.666, respectively. The scatter in $\langle \mu \rangle_{\rm sim}$ can be attributed to the "cosmic" variance. The fact that $\langle \mu \rangle_{\rm sim}$ is on average slightly lower than its theoretical value arises since we consider finite regions in the deflector plane and in the source plane. Rays that fall very close to a star in our deflector field suffer very large deflection angles, which may take them outside of our source field; these are not compensated for by rays with large deflection angles from stars outside of our deflector field that should have been deflected into our source field (see Katz, Balbus, & Paczyński 1986; Schneider & Weiss 1987). We conclude that the numerical simulations are in good agreement with the theory on the value of $\langle \mu \rangle$ as well.

The magnification distribution of the macroimage (MDM) $p(\mu)$, where $p(\mu)\, d\mu$ is the probability that the total magnification of the macroimage is between μ and $\mu + d\mu$, can be expressed as a sum over the contributions from regions with different numbers of EIPs n,

$$p(\mu) = \sum_{n=0}^{\infty} p_n(\mu) \; , \qquad (11)$$

where $p_n(\mu)\, d\mu = (dp_n/d\mu)\, d\mu$ is the probability of having n EIPs and a total magnification between μ and $\mu + d\mu$, with the normalization

$$\int_0^{\infty} p_n(\mu)\, d\mu = p_n , \qquad \int_0^{\infty} p(\mu)\, d\mu = 1 \; . \qquad (12)$$

In Figure 3 we show the results for p_n from our simulations (which are given in Table 2), along with a Poisson
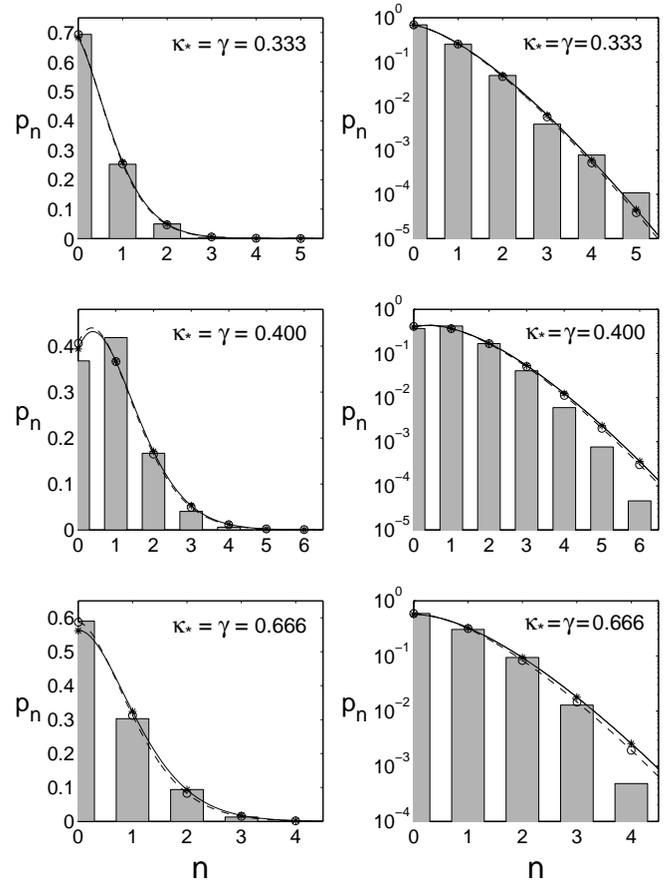

FIG. 3.—Bars show the probability p_n of having n EIPs, calculated from our simulations ($\kappa_* = \gamma = 0.333$, 0.400, and 0.666) using eq. (9). The lines correspond to a Poisson distribution (eq. [13]), where the solid line is for the analytical (theoretical) mean value $\langle n \rangle$ and the dashed line is for the mean value from the simulation $\langle n \rangle_{\rm sim}$, calculated according to eq. (10). The theoretical values of p_n for integer values of n are shown by the asterisks and circles. The panels on the left are linear representations of p_n, while those on the right are logarithmic.

distribution,

$$p_n = \frac{e^{-a} a^n}{n!} \; , \qquad (13)$$

where the solid line is for $a = \langle n \rangle$ and the dashed line is for $a = \langle n \rangle_{\rm sim}$, calculated according to equation (10). A Poisson distribution provides a reasonable fit to the results of all our simulations. For large values of n there is a relatively larger deviation from a Poisson distribution. This results, in part, from the difficulty in identifying regions with large n in the source plane. One should also keep in mind that the "cosmic" variance in p_n becomes larger with increasing n. There still seem to be some systematic deviations from a Poisson distribution; however, they appear to be small for relatively low values of n, which cover most of the source plane. We therefore consider a Poisson distribution for p_n to be a reasonable approximation.

Figure 4 shows plots of $\mu p(\mu)$ and $\mu p_n(\mu)$ from our simulations. The shapes of $p_n(\mu)$ for different n seem quite similar, while the average magnification

$$\langle \mu \rangle_n = \frac{1}{p_n} \int_0^{\infty} p_n(\mu) \mu\, d\mu \qquad (14)$$
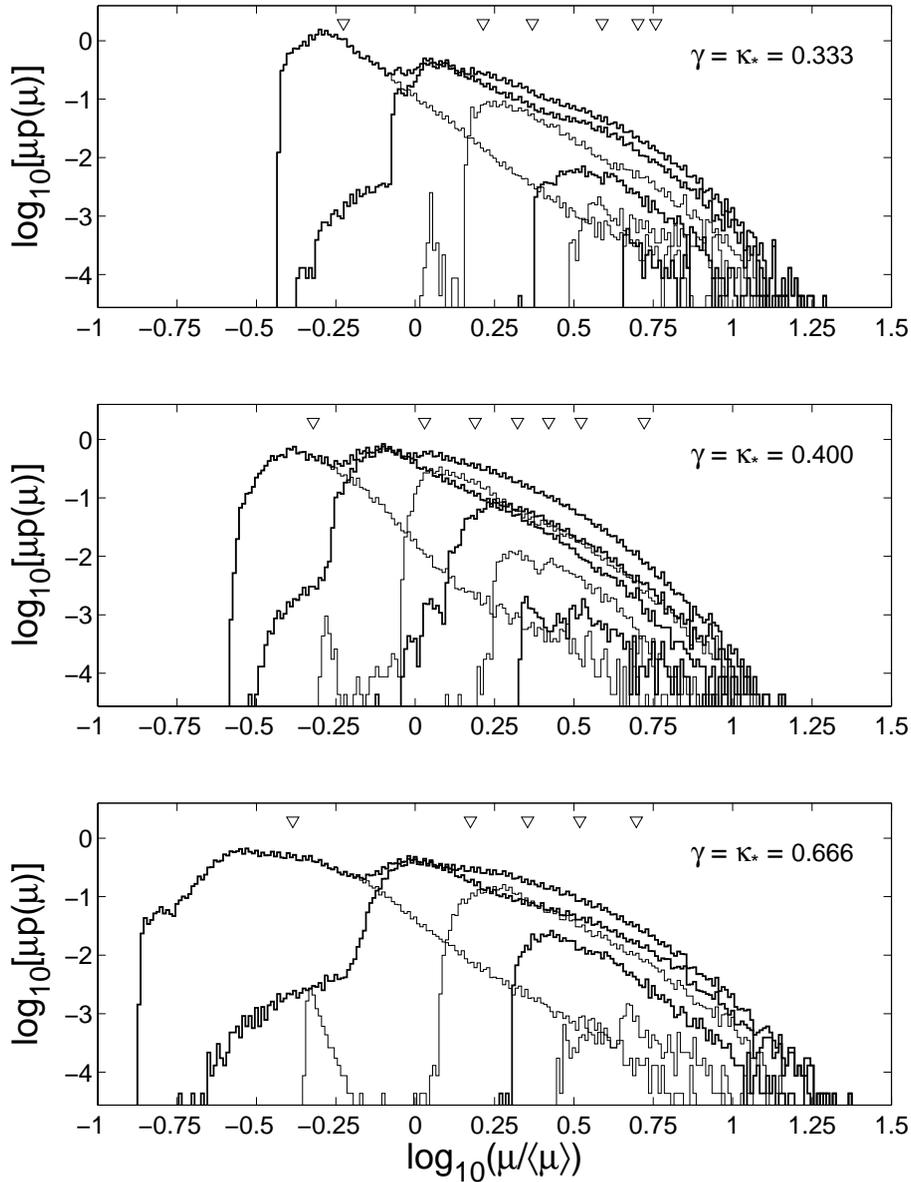
and the normalization p_n are different.

Fig. 4.—A log-log plot of the magnification distribution for the macroimage (MDM) $\mu p(\mu)$ (*top line*) for our simulations and its decomposition $\mu p_n(\mu)$ to the contributions from regions with different numbers of extra microimage pairs (EIPs) n. The alternating thin and thick solid lines, from left to right, are for $n = 0$–6. The inverted triangles represent the average magnification from regions with n EIPs, $\langle \mu \rangle_n$.

4. DISCUSSION

We have calculated the mean number of extra micro-image pairs (EIPs) $\langle n \rangle$ of a point source as a function of κ_* and γ. The results are shown in Figure 1 and Table 1. One-dimensional integrals for general values of (κ_*, γ) and an analytic result for the case $\gamma = \kappa_*$ are presented in the Appendix. Near the lines of infinite magnification in the γ-κ_* plane ($\gamma = |1 - \kappa_*|$), $\langle n \rangle$ diverges and is proportional to the mean macromagnification $\langle \mu \rangle$. The ratio $\langle n \rangle / \langle \mu \rangle$ is continuous along these lines and varies smoothly along the line $\gamma = \kappa_* - 1$, while its derivative is discontinuous along the line $\gamma = 1 - \kappa_*$ in directions that are not along this line. This creates a "ridge" in $\langle n \rangle / \langle \mu \rangle$ along the line $\gamma = 1 - \kappa_*$, where it also peaks at $(\kappa_*, \gamma) = (0.379, 0.621)$ with $(\langle n \rangle / \langle \mu \rangle)_{\max} = 0.306$. The analytic results for $\langle n \rangle$ are in good agreement with the results of

numerical simulations we performed for $\kappa_* = \gamma = 0.333$, 0.400, and 0.666 (as can be seen in Table 2).

We find that the probability distribution p_n for the number of EIPs n, which is calculated from numerical simulations, can be reasonably described by a Poisson distribution. This result holds for both the numerical simulations performed in this paper (e.g., Table 3 and Figs. 2 and 3) and numerical simulations from previous works (Rauch et al. 1992). Furthermore, the shape of the magnification distribution $p_n(\mu)$ of regions with a given n appears to be similar for different values of n, where only the overall normalization p_n and mean magnification $\langle \mu \rangle_n$ depend on n (see Fig. 4).

The mean number of EIPs $\langle n \rangle$ can serve as a rough measure for the width of $p(\mu)$, the magnification distribution for the macroimage (MDM). For $\langle n \rangle \ll 1$ there is little contribution to the MDM from regions in the source plane with $n > 0$, since these regions cover only a small fraction of the

source plane. For $\langle n \rangle \gg 1$ the Poisson distribution p_n for n approaches a Gaussian distribution with a mean value of $\langle n \rangle$ and a standard deviation of $\sigma = \langle n \rangle^{1/2}$, so that only $\sim \langle n \rangle^{1/2}$ different values of n around $n \approx \langle n \rangle$ have a noticeable contribution to the MDM. We also note that the average magnification from regions with n EIPs, $\langle \mu \rangle_n$, is approximately linear in n (see Table 3), so we expect $\Delta \mu / \langle \mu \rangle \sim \langle n \rangle^{-1/2} \ll 1$. Therefore, the width of the MDM is expected to be largest for $\langle n \rangle \sim 1$. This seems to be in rough agreement with the results of numerical simulations (Wambsganss 1992; Lewis & Irwin 1995; Schechter & Wambsganss 2002).

APPENDIX

ANALYTIC EXPRESSIONS FOR PRIVATE CASES

The inner integral in equation (6) can be solved analytically, reducing it to a single integral:

$$\frac{\langle N \rangle}{\langle \mu \rangle} = \frac{\kappa_*}{2\pi} \int_{-1-\gamma}^{1-\gamma} dS_1 \left[\ln\left(\frac{A-B}{A+B}\right) + \frac{2AB}{(\kappa_*^2 + S_1^2)} \right], \tag{A1}$$

where $\langle \mu \rangle = |(1 - \kappa_*)^2 - \gamma^2|^{-1}$ (see eq. [3]) and

$$A \equiv \sqrt{1 + \kappa_*^2 - \gamma(2S_1 + \gamma)}, \qquad B \equiv \sqrt{1 - (S_1 + \gamma)^2}. \tag{A2}$$

This integral can be easily evaluated numerically. Alternatively, changing variables in equation (6) to r and ϕ, where $x = \gamma + S_1, y = S_2, r^2 = x^2 + y^2$, and $\tan(\phi) = y/x$, gives

$$\frac{\langle N \rangle}{\langle \mu \rangle} = \frac{\kappa_*}{2\pi} \int_0^1 dr \int_0^{2\pi} d\phi \, \frac{r(1-r^2)}{(\kappa_*^2 + \gamma^2 + r^2 - 2\gamma r \cos\phi)^{3/2}} = \frac{2\kappa_*}{\pi} \int_0^1 dr \, \frac{r(1-r^2)E\left(\pi/2, \, -4\gamma r / \left[\kappa_*^2 + (r-\gamma)^2\right]\right)}{\left[\kappa_*^2 + (r+\gamma)^2\right]\sqrt{\kappa_*^2 + (r-\gamma)^2}}, \tag{A3}$$

where

$$E(\phi, \, x) \equiv \int_0^\phi d\theta \, (1 - x \sin^2 \theta)^{1/2}. \tag{A4}$$

For the case of $\gamma = \kappa_*$, corresponding to a singular isothermal sphere, we obtain an analytic result:

$$\frac{\langle N \rangle}{\langle \mu \rangle} = \frac{1}{\sqrt{\gamma}\pi} \left\{ -6\gamma^2 E\left(\arcsin(C), \, C^{-2}\right) - 3(1-\gamma)\gamma^2 F\left(\arcsin(C), \, C^{-2}\right) \right. $$
$$\left. + C\left[\gamma(2\gamma^2 - 1)K(C^2) + D\Pi(E, C^2) + D^*\Pi(E^*, C^2)\right] \right\}, \tag{A5}$$

where

$$C \equiv \sqrt{\frac{4\gamma}{1 + 2\gamma + 2\gamma^2}}, \qquad D \equiv \frac{i + (1-i)\gamma + (2-i)\gamma^2 - (1+3i)\gamma^3}{4}, \qquad E \equiv \frac{2}{1 + (1+i)\gamma}, \tag{A6}$$

D^* and E^* are the complex conjugates of D and E, and

$$F(\phi, \, x) \equiv \int_0^\phi d\theta \, (1 - x \sin^2 \theta)^{-1/2}, \qquad K(x) \equiv F\left(\frac{\pi}{2}, \, x\right),$$

$$\Pi(x, \, y) \equiv \int_0^{\pi/2} d\theta \, (1 - x \sin^2 \theta)^{-1} (1 - y \sin^2 \theta)^{-1/2}. \tag{A7}$$

REFERENCES

Burud, I., et al. 1998, A&A, 339, 701
Chang, K., & Refsdal, S. 1979, Nature, 282, 561
Chiba, M. 2002, ApJ, 565, 17
Corrigan, R. T., et al. 1991, AJ, 102, 34
Dalal, N., & Kochanek, C. S. 2002, ApJ, 572, 25
Garnavich, P. M., Loeb, A., & Stanek, K. Z. 2000, ApJ, 544, L11
Gaudi, B. S., Granot, J., & Loeb, A. 2001, ApJ, 561, 178
Gil-Merino, R., Wisotzki, L., & Wambsganss, J. 2002, A&A, 381, 428

Hewitt, J. N., Turner, E. L., Lawrence, C. R., Schneider, D. P., & Brody, J. P. 1992, AJ, 104, 968
Inada, N., et al. 2002, ApJ, submitted
Irwin, M. J., Webster, R. L., Hewett, P. C., Corrigan, R. T., & Jedrzejewski, R. I. 1989, AJ, 98, 1989
Jackson, N. J., Xanthopoulos, E., & Browne, I. W. A. 2000, MNRAS, 311, 389
Katz, N., Balbus, S., & Paczyński, B. 1986, ApJ, 306, 2

Koopmans, L. V. E., & Wambsganss, J. 2001, MNRAS, 325, 1317
Lawrence, C. R., Elston, R., Januzi, B. T., & Turner, E. L. 1995, AJ, 110, 2570
Lewis, G. F., & Irwin, M. J. 1995, MNRAS, 276, 103
———. 1996, MNRAS, 283, 225
Lewis, G. F., Irwin, M. J., Hewett, P. C., & Foltz, C. B. 1998, MNRAS, 295, 573
Mao, S., & Scneider, P. 1998, MNRAS, 295, 587
Metcalf, R. B., & Madau, P. 2001, ApJ, 563, 9
Nityananda, R., & Ostriker, J. P. 1984, J. Astrophys. Astron., 5, 235
Østensen, R., et al. 1997, A&AS, 126, 393
Paczyński, B. 1986, ApJ, 301, 503
Pelt, J., Schild, R., Refsdal, S., & Stabell, R. 1998, A&A, 336, 829
Rauch, K. P., Mao, S., Wambsganss, J., & Paczyński, B. 1992, ApJ, 386, 30
Reimers, D., Hagen, H. J., Baade, R., Lopez, S., & Tytler, T. 2002, A&A, 382, L26
Schechter, P. L., & Moore, C. B. 1993, AJ, 105, 1
Schechter, P. L., & Wambsganss, J. 2002, ApJ, 580, 685
Schechter, P. L., et al. 2003, ApJ, in press
Schild, R. 1996, ApJ, 464, 125
Schneider, P., Ehlers, J., & Falco, E. E. 1992, Gravitational Lenses (Berlin: Springer)
Schneider, P., & Weiss, A. 1987, A&A, 171, 49

Schneider, P., & Weiss, A. 1988, ApJ, 327, 526
Trotter, C. S., Winn, J. N., & Hewitt, J. N. 2000, ApJ, 535, 671
Wambsganss, J. 1990, Ph.D. thesis, Ludwig-Maximilians-Univ., Munich
———. 1992, ApJ, 386, 19
———. 1999, J. Comput. Appl. Math., 109, 353
———. 2001, Publ. Astron. Soc. Australia, 18, 207
Wambsganss, J., Paczyński, B., & Schneider, P. 1990, ApJ, 358, L33
Wambsganss, J., Schmidt, R., Colley, W., Kundić, T., & Turner, E. L. 2000, A&A, 362, L37
Wambsganss, J., Witt, H. J., & Schneider, P. 1992, A&A, 258, 591 (WWS92)
Witt, H. J. 1993, ApJ, 403, 530
Woźniak, P. R., Alard, C., Udalski, A., Szymański, M., Kubiak, M., Pietrzyński, G., & Zebruń, K. 2000a, ApJ, 529, 88
Woźniak, P. R., Udalski, A., Szymański, M., Kubiak, M., Pietrzyński, G., Soszyński, I., & Zebruń, K. 2000b, ApJ, 540, L65
Wyithe, J. S. B., & Loeb, A. 2002, ApJ, 577, 615
Wyithe, J. S. B., & Turner, E. L. 2002, ApJ, 567, 18
Wyithe, J. S. B., Webster, R. L., Turner, E. L., & Mortlock, D. J. 2000, MNRAS, 315, 62
Yonehara, A. 1999, ApJ, 519, L31
———. 2001, ApJ, 548, L127
Young, P. 1981, ApJ, 244, 756